ARTICLE

Check for updates

Randomly stacked open cylindrical shells as functional mechanical energy absorber

Tomohiko G. Sano [1,3✉], Emile Hohnadel[2,3], Toshiyuki Kawata[1], Thibaut Métivet[2] & Florence Bertails-Descoubes [2✉]

Structures with artificially engineered mechanical properties, often called mechanical meta-materials, are interesting for their tunable functionality. Various types of mechanical meta-materials have been proposed in the literature, designed to harness light or magnetic interactions, structural instabilities in slender or hollow structures, and contact friction. However, most of the designs are ideally engineered without any imperfections, in order to perform deterministically as programmed. Here, we study the mechanical performance of randomly stacked cylindrical shells, which act as a disordered mechanical metamaterial. Combining experiments and simulations, we demonstrate that the stacked shells can absorb and store mechanical energy upon compression by exploiting large deformation and relocation of shells, snap-fits, and friction. Although shells are oriented randomly, the system exhibits statistically robust mechanical performance controlled by friction and geometry. Our results demonstrate that the rearrangement of flexible components could yield versatile and predictive mechanical responses.

[1] Department of Mechanical Engineering, Keio University, Yokohama 2230061 Kanagawa, Japan. [2] INRIA, CNRS, Université Grenoble Alpes, INP, LJK, Grenoble 38000, France. [3]These authors contributed equally: Tomohiko G. Sano, Emile Hohnadel. ✉email: sano@mech.keio.ac.jp; florence.descoubes@inria.fr

Predicting the large deformation of slender structures, such as pillars, beams, and arches, is one of the central issues in Material Science[1]. By forecasting structural instability and optimising their design to prevent rupture, slender parts can be assembled into lasting architectural buildings, easier to build and able to withstand large external forces, thereby resilient to natural disasters. Engineers design energy- or force-absorbing structures to protect humans and objects from impact or shocks. Examples include bicycle helmets and packaging materials for fragile baggage[2]. The energy- or force-absorbing structures are often soft elasto-plastic multiscale materials, carefully designed at the structural and chemical levels, to control the deformation modes.

When a slender beam is compressed axially, it bends and buckles, as bending is more energetically favourable than compression[3,4]. The buckling of a slender beam can be regarded as a classical and canonical example of a—reversible—energy-absorbing phenomena[5]. The beam bends and buckles when subjected to forces beyond Euler's critical load, and the external energy is then stored as bending energy. The stored energy can thereafter be released by removing the external load. Hence, the instability of slender structures could be interpreted as a mechanical energy transducer[5]. This idea has been part of the recent evolution of materials and structures with an artificial mechanical response, called mechanical metamaterials[6].

Recent progress in fabrication technology and computational modelling have also fostered the investigation of tunable mechanical functionality. Various types of mechanical responses have been studied, such as auxetics[7,8], friction-dominated assemblies[9], snapping[10–12], twist-extension coupling[13], elasto-magnetic coupling[14], or origamis and kirigamis[15]. Mechanical metamaterials however usually require accurate engineering to achieve the programmed responses[16]. The effects of randomness and imperfection of the components on the mechanical performances are seldom clarified, although these factors are likely to manifest all the more as the diversity and local arrangement of the structures at play constantly increase.

In this article, we report the mechanical properties of randomly stacked open cylindrical shells, combining experiments and simulations (see Fig. 1a). We carefully fabricate open cylindrical thin shells whose rest geometry (inset in Fig. 1c) is an extruded surface characterised by a radius R and a shell angle Φ, the thickness h being negligible compared to the shell arc length ΦR. Each shell deforms elastically in 2D and interacts with other shells through contact and friction. We then consider a stack of identical shells placed in a random 2D configuration (see Fig. 1a). This heterogeneous system exhibits characteristic damping against compression, supplemented by friction, elastic bending, and shell reorientation. Upon compression, shells interact and may suddenly overlap, a phenomenon called snap-fit. These snap-fit events irreversibly reduce local empty spaces and voids, thereby lowering the overall compressive load. Furthermore, frictional contacts induce further dissipation throughout the cycle. As will be shown, although the initial configuration of our system is set randomly, energy dissipation remains nearly constant across statistical sampling, while compressibility turns out to be tunable by the shell geometry. Our work is complementary to the pioneering work by Poirier et al.[17], where the localised deformation of stacked straws is studied purely experimentally.

Results

Experimental results overview. Randomly stacked open cylindrical shells of identical geometry are compressed and decompressed. In the absence of any external load ($F = 0$), empty spaces still exist between the shells, which gives rise to a porous structure, contributed by both friction and elasticity (Fig. 1a). Upon compression, the load F increases with large deformation of the
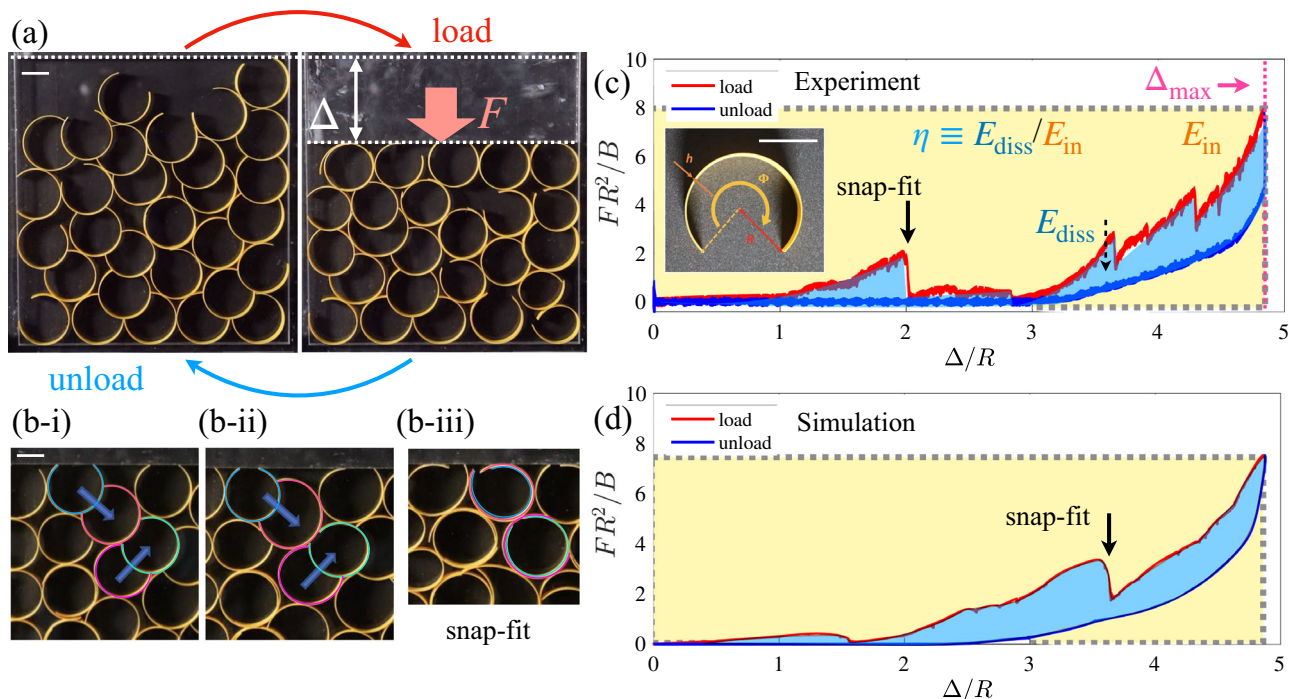
Fig. 1 Mechanics of randomly stacked open cylindrical shells with shell angle Φ. a Our base experiment, where the randomly stacked shells are compressed and then decompressed. **b-i** to **b-iii** The load F is absorbed into the elastic deformation with F decreasing when shells embrace each other (snap-fit). **c, d** The typical force-displacement curve upon compression (red) and decompression (blue) in **c** experiments and **d** simulations. Note that the experimental and numerical force-displacement curves were picked to be illustrative and similar to each other, among all of the possible outputs yielded by the same physical parameters but random initial configurations (see Fig. 5a). As such, they do not necessarily reflect the statistically averaged quantities analysed below. The black arrows highlight the snap-fit force drops in load F (scale bars 20 mm).

shells, followed by force drops corresponding to (local) inter-mittent snap-fits. As we compress the system further, the increase and decrease of the compression force continue up to the end of the test (Fig. 1b–d).

Elementary two-shell snap-fit. The observed drops of the force F find their origin in local snap-fit phenomena involving two open shells, where one shell embraces the other. To understand this elementary process, we consider a compression test between two identical shells with varying shell angle Φ. When two identical shells are assembled, they snap either smoothly or abruptly, depending on the friction coefficient μ and the shell angle Φ. We call the former and the latter modes Type I and II snap-fits, respectively, following the classification that Yoshida et al.[12] pro-posed in the case of a shell indenting a rigid cylinder. In the Type I snap-fit, the upper indenting shell continuously slides on the bot-tom one, passing the smooth peak force $f_{\text{Type I}} \sim 0.1 B/R^2$ (with B the bending modulus of the shell), until the indentation exceeds the shell radius, when the force becomes negative and the shells naturally snap-fit each other. The Type II behaviour, which can be observed for more closed shells, on the contrary, features sticking and coiling of the upper shell, until the force reaches the threshold, and the shell abruptly unfolds onto the other. Note that the Type II threshold force is much higher—$f_{\text{Type II}} \sim 5B/R^2 \gg f_{\text{Type I}}$—than the typical forces for Type I events. In ref. [12], the shell-cylinder problem is studied with different diameter ratios, leading to either snap-fit or misfit, where the shell cannot fit onto the cylinder. However, given that we consider two identical shells, our shells always snap-fit, and we only consider Type I and II snap-fits throughout.

We investigate the two-shell elementary process both experi-mentally and numerically (see Fig. 2). Due to its 2D nature, and considering the negligible thickness h of the shells, the two-shell assembly scenario can be simulated using 2D thin elastic rods, under the unshearable and inextensible assumptions of the Kirchhoff rod theory. To this end, we develop an unclamped, 2D version of the Super-Helix model for discrete Kirchhoff rods[18] with a full account of dry frictional contact[19]. In section

'Simulations' we provide a detailed description of our rod simulator augmented with frictional contact, which has been recently validated in 2D and 3D[20], in particular on the 2D pinning test[21], which couples elasticity and frictional contact. We run a new validation test, by comparing our simulator to the analytical master curve of Yoshida et al.[12] (Supplementary Fig. 1). An excellent agreement is observed here again between theory and simulation, which paves the way for the extensive parametric studies performed below with our simulator.

Using exhaustive simulations, we explore the phase diagram of the shell-shell snap-fit, and find, similarly to the shell-cylinder analysis of Yoshida et al.[12], that both the friction coefficient μ and the shell geometry Φ impact the snapping behaviour between two identical shells. As summarised in Fig. 2c, the larger μ or Φ, the more Type II snap-fit happens. Between the Type I and II regimes, there exists a critical shell angle $\Phi^* = \Phi^*(\mu)$, which decreases as μ increases. Experimentally, we similarly find out a transition between Type I and II regimes, as Φ varies. These experimental and numerical results highlight the fact that not only the friction between shells but also their geometric non-linearity plays a critical role in the mechanical performance of stacked shells. Furthermore, it is noteworthy that thanks to its monotonic dependence, the critical angle $\Phi^*(\mu)$ can be exploited to determine accurately the friction coefficient between our experimental shells by measuring the actual threshold angle between the Type I and II, as explained in Fig. 2.
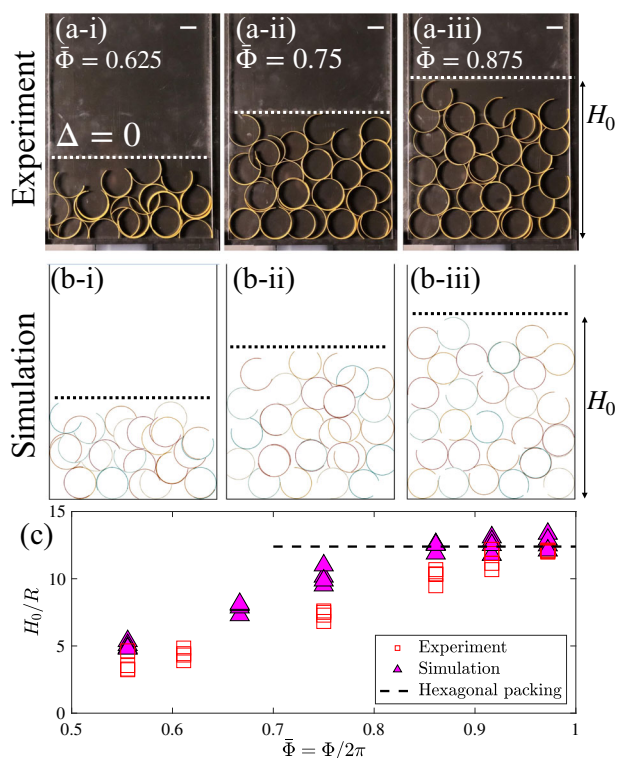
In the remainder of the paper, we thus use this experimental measurement to bound the friction coefficient $0.32 \leq \mu \leq 0.41$ and use $\mu = 0.35$ in all our simulations (two-shell and many-shell) when comparing with the experiments. With this μ fixed, we thus classify our experimental shells into two categories depending on their normalised angle $\bar{\Phi} \equiv \Phi/(2\pi)$: Type I shells for $\bar{\Phi} < \bar{\Phi}^*(0.35)$, and Type II shells for $\bar{\Phi} \geq \bar{\Phi}^*(0.35)$, with $\bar{\Phi}^*(0.35) = 0.83$.

Many-shell snap-fit. We consider sets of $N = 30$ systematically fabricated shells with various Φ values (all other parameters remaining fixed) and stack them randomly inside a container
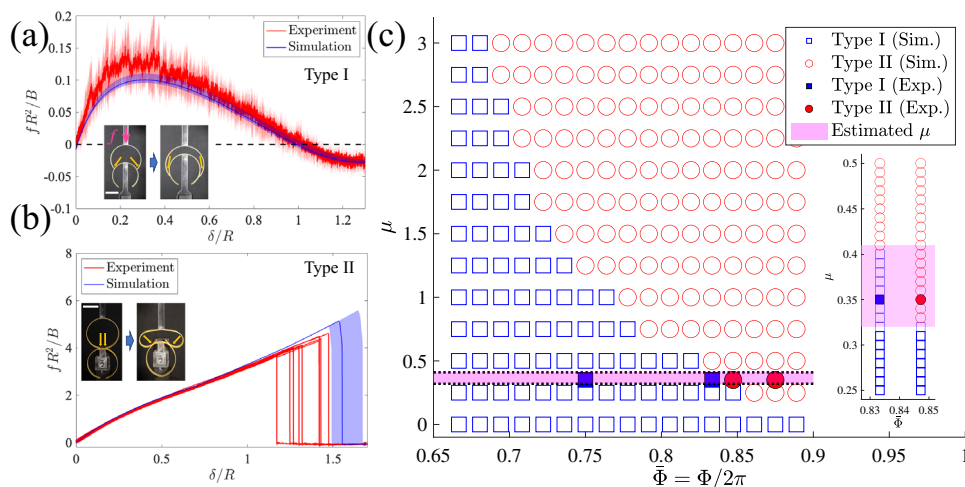
Fig. 2 How an elastic shell snaps onto a second identical shell. a, b Rescaled force-displacement curves for **a** Type I and **b** Type II snapping regimes, where the red and blue curves are experimental and simulation results, respectively. The blue shaded regions represent the error bars against our estimate of the experimental friction coefficient, $0.32 \leq \mu \leq 0.41$ (scale bars 20 mm). **c** Phase diagram of the shell deformation on the $(\Phi/2\pi)$–μ plane, where empty data points are simulation results. Similarly to the shell-cylinder problem studied by Yoshida et al.[12], the diagram shows the existence of a monotonic critical angle function $\Phi^*(\mu)$ separating the Type I regime (in blue squares) from the Type II regime (in red circles). In parallel, experiments made for various controlled shell angles Φ—but for an unknown friction coefficient μ— lead either to Type I or Type II outcomes (filled data points): this experimental capture of regime change allows us to identify precisely the range of possible values for the experimental friction coefficient μ (shaded region) as the interval $[0.32-0.41]$, where the simulated Type I and II phase boundary coincides with the experimental one. In our simulations, we then systematically take $\mu = 0.35$ when comparing to experimental data. The corresponding normalised critical angle is then given by $\bar{\Phi}^*(0.35) = 0.83$.

under the effect of gravity (c.f. Fig. 3a, b for typical static configurations). The exact same scenario is replicated with simulation, randomly initialising the position and orientation of each of the 30 rings, before applying gravity and having them fall into a virtual container. The friction coefficient between the rings and the container is set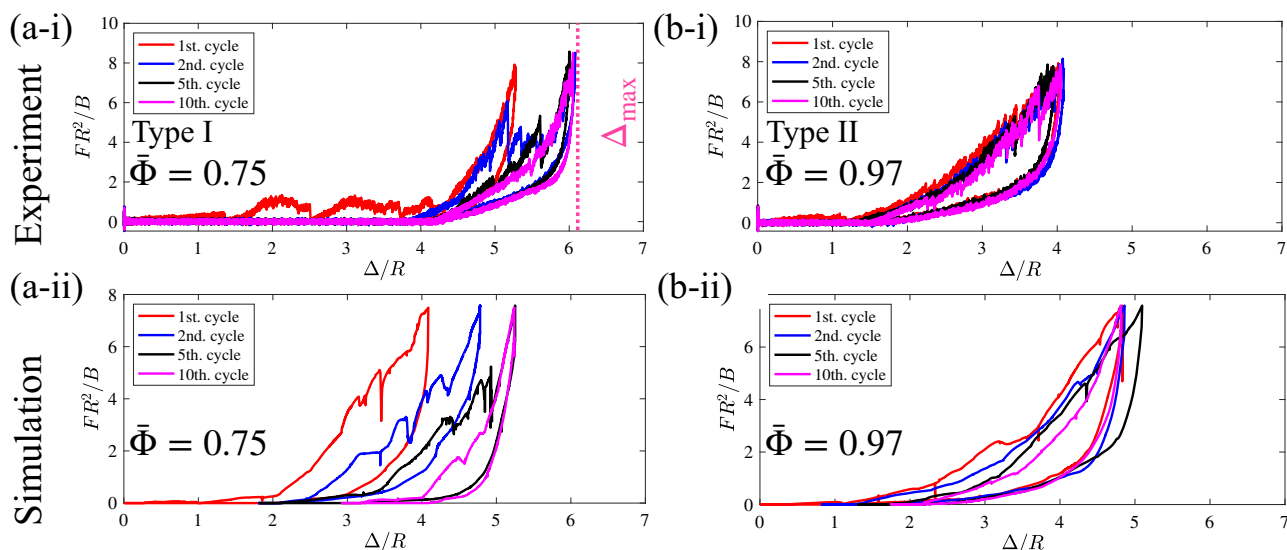 to 0.35, similar to the ring-ring friction coefficient. Unlike the latter coefficient (ring-ring), however, we note in practice that the former has little influence on the overall stack behaviour.

It is noteworthy that the geometry of the shells controls the height of the full system when stacked. Indeed, the initial height of the stacked shells, H_0, monotonically increases with Φ and saturates to the height corresponding to the hexagonal packing $H_0/R \to 2 + 6\sqrt{3}$ as $\Phi \to 2\pi$. We observe that the simulation correctly captures the experimental and expected behaviour for H_0.

To further analyse the mechanical properties of the stacked shells, we perform cyclic compression-decompression experiments and simulations. The forces and displacement are respectively normalised by the characteristic bending force B/R^2 and relocation length R. The stacked shells are compressed by a rigid plate from $\Delta \equiv H_0 - H = 0$, up to the point where the force exerted on the plate reaches some maximal value $F = F_{max}$. The material is then decompressed back to $\Delta = 0$ (see Fig. 4a, b). In practice, we use $F_{max} = 5$ N throughout the experiments and simulations, to yield as many snap-fits as possible while ensuring that we remain much below the plasticity and rupture thresholds of the shells. Simulations give results fully consistent with the experiments, as detailed below.

When we start compressing the stacked Type I shells ($\bar{\Phi} < 0.83$), in the first $n = 1$ cycle the compressive load exhibits a characteristic damping behaviour: the force F increases as the shells bend, and then drops abruptly as snap-fit events occur within the system (Fig. 4a-i, a-ii and Supplementary Movie 1). The continued compression causes snap-fits throughout the system. A pair of overlapped shells could be regarded as a shell of double thickness $2h$, thus increasing the (effective) bending stiffness and stiffening the overall system. As a result, F increases rapidly as we compress. Upon decompression, the assembled shells often do not separate into two, so that F gets relaxed to zero smoothly. The compression and decompression process is as such fully irreversible. For the second $n = 2$ and subsequent cycles, snap-fit is less and less likely to happen, because the force required for the Type I snap-fit $f_{Type\,I} \approx 0.06$ N is much lower than F_{max}: $F_{max} \gg f_{TypeI}$. In other words, most of the possible snappable pairs have already snapped after the 1st compression. As the cycle continues $n \gg 1$, the force-displacement curve converges to a limit cycle curve, where elastic bending of the shells and frictional sliding between them are dominant.

Fig. 3 Static properties of randomly stacked shells under gravity (before compression). Configurations of shells obtained from **a-i** to **a-iii** experiments and **b-i** to **b-iii** simulations with various Φ. **c** Normalised height (prior to compression), H_0/R, as a function of Φ. Red squares and magenta triangles are experimental and simulation data, respectively (scale bars 20 mm).

Fig. 4 Dynamic properties of 30 randomly stacked shells. Force-displacement curve for Type I ($\bar{\Phi} = 0.75$) (**a-i** and **a-ii**) and Type II shells ($\bar{\Phi} = 0.97$) (**b-i** and **b-ii**). As the number of cycles increases, the curve converges to a limit cycle loop, that is reached much more quickly for Type II shells. We show the corresponding curves for the 1st (red), 2nd (blue), 5th (black) and 10th (magenta) cycle in each panel.

In contrast, when we compress the stacked Type II shells ($\bar{\Phi} \geq 0.83$), the force-displacement curve is qualitatively different from that of Type I shells. Interestingly, we do not observe Type II snap-fit in this problem set, despite that the compressive force is higher than the Type II threshold: $f_{\text{TypeII}} \sim 5B/R^2 \simeq 3.13 \, \text{N} < F_{\text{max}}$ (Fig. 4b-i, b-ii and Supplementary Movie 2). As we observe in the two-shell snap-fit, the Type II shell sticks, rolls and then unfolds upon compression, requiring much space for its large deformation. However, surrounding shells prevent opening the shell. In other words, the compression induces elastic bending and sliding only. As a result, the limit force-displacement cycle curve is basically immediately reached. This qualitative difference in the mechanical performance of stacked shells originates not only from the elasticity and geometry of each shell but also from contact mechanics and rearrangement of shells.

In both Type I and Type II cases, the limit force-displacement cycle exhibits a characteristic dissipation hysteresis which is reminiscent of other thin elastic systems coupled with frictional contact[22]. To understand the dissipative properties of this system quantitatively, we compute the maximum working distance, Δ_{max}, and the dissipation ratio η (defined below) in our $N = 30$ shells experiments and simulations. To mitigate the effect of the initial conditions for small-size systems, assuming ergodicity of the system, we perform independent measurements with respectively 5 and 100 different random initial configurations for the experiments and simulations. In addition, we compute the robust normalised mean absolute deviation, as it decreases the bias of potential outliers[23]. In the following, we restrict the analysis to the first $n = 1$ cycle, where the snap-fit effects are more pronounced and characteristic than the limit cycles ($n \geq 2$).

The maximum working distance Δ_{max} represents the displacement between the initial height H_0 and the final height when F reaches the prescribed maximum force F_{max}. As shown in Fig. 5a, c, two regimes can be identified for Δ_{max} depending on the shell opening angle Φ, with respect to the critical angle Φ^* (separating the type I and type II regimes in the shell-on-shell case as shown in Fig. 2):

- $\Phi < \Phi^*$: as discussed above, the type I-shell system is subjected to snap-fit events, and the more closed the shells, the larger Δ_{max}, as the more snap-fits—and thus force drops—occur during the compression.

- $\Phi \geq \Phi^*$: for type II shells, snap-fits no longer happen as type II snap-fit unrolling is blocked by confinement, as discussed above; the system is thus driven by shell bending, and mutual and self-contact sliding interactions, and the more closed the shells, the stiffer the bending response (due to the earlier happening of self-contact), which leads to larger forces and thus a decrease of the Δ_{max} required to reach F_{max}.

From a more functional perspective, the ability to tune Δ_{max} with the shell geometry Φ could be useful in order to program the compression properties on demand.

In addition to Δ_{max}, we measure the dissipation ratio, η, defined as the area of the hysteretic F-Δ curve, $E_{\text{diss}} \equiv \oint F d\Delta$, normalised by the total energy input $E_{\text{in}} \equiv F_{\text{max}}\Delta_{\text{max}}$: $\eta \equiv E_{\text{diss}}/E_{\text{in}}$. Despite the qualitative differences observed between small-Φ and large-Φ $F - \Delta$ curves, the dissipation ratio η turns up to be independent on the opening angle Φ (Fig. 5b). We can therefore conclude that the stacked assembly exhibits robust energy-dissipating performance.

The results from the simulations at $\mu = 0.35$ are in excellent agreement with the experimental $(\Delta_{\text{max}}, \eta)$ (Fig. 5a, b and Supplementary Movie 3). Given the prior validation of our numerical method on shell-on-shell experiments, in the following, we fully rely on numerical simulations to study the role of the friction coefficient μ.
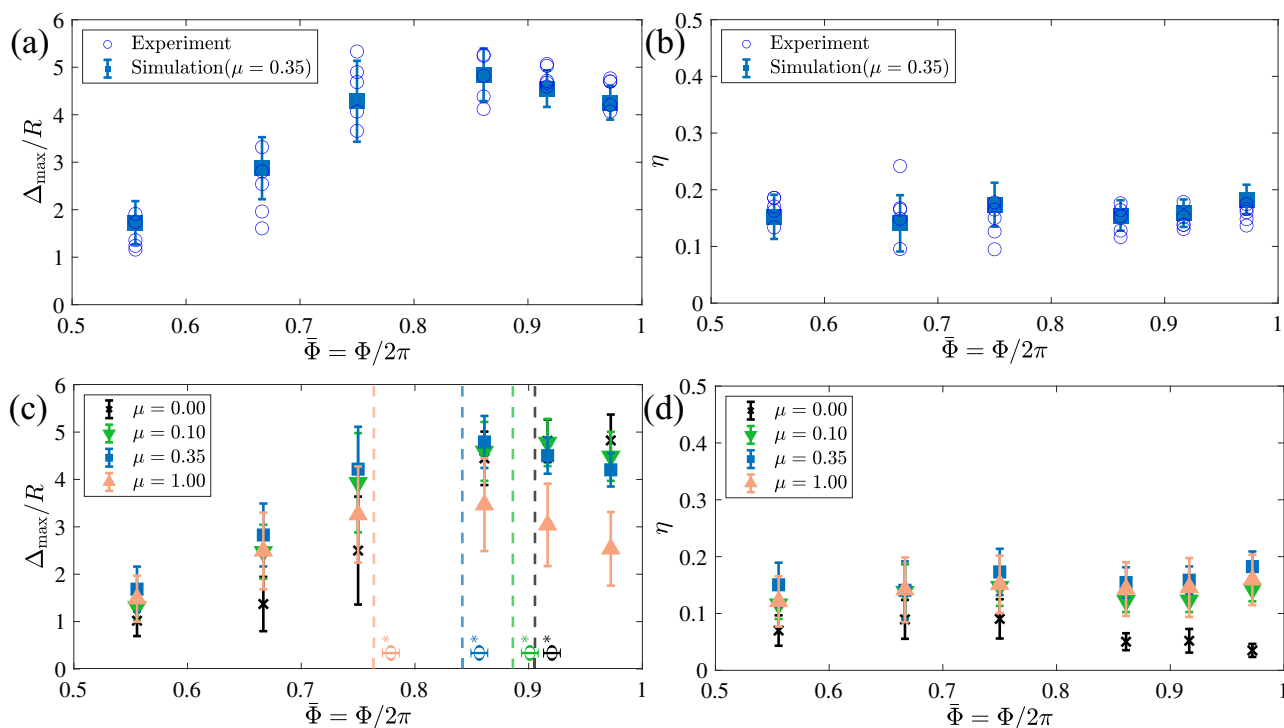
Fig. 5 The maximum relative displacement, Δ_{max} and energy absorption ratio, η as a function of (Φ, μ). Experimental and simulation results are superposed. Experiment results (blue empty circles) for **a** Δ_{max} and **b** η, plotted against Φ as open symbols. The corresponding simulation results (blue filled squares) for different friction coefficients ($\mu = 0.35$) are plotted as filled symbols. Simulation results of **c** Δ_{max} and **d** η for different friction coefficients ($\mu = 0.00, 0.10, 0.35, 1.0$, black, green, blue, yellow, respectively). The error bars represent the median absolute deviation over the samples. The vertical dashed lines in (**c**) indicate the respective critical Φ^* for the different values of μ.

To evaluate the role of friction in the mechanical and dissipative performances of the system, we carry out numerical simulations for smaller (starting from $\mu = 0.0$) and larger (up to $\mu = 1.0$) friction coefficients, while other parameters remain the same (as before, the friction coefficient between the rings and the container is set to the ring-ring μ value). See Supplementary Movie 4 for comparison. The results for (Δ_{max}, η) are summarised in Fig. 5c, d, respectively. While Δ_{max} seems independent of μ for wide open ($\bar{\Phi} \lesssim 0.75$) shells, it decreases as μ increases for more closed shells. This observation can be interpreted in the limit regimes of either wide open ($\Phi \rightarrow \pi$), or nearly closed ($\Phi \rightarrow 2\pi$) shells: in the first case, the system is in the type I regime, and is mostly driven by snap-fit events between the shells; Δ_{max} is therefore controlled by the geometry of the system, which affects the total number of possible snap-fits. Friction plays no role in this limit case, and the maximal indentation is thus independent on μ. On the contrary, as shells become nearly closed, no snap-fit happens anymore, and the frictional mutual interactions are expected to become dominant: increasing the friction coefficient μ thus naturally leads to an increase of the force response of the system during compression (see Supplementary Note 3)—as the Coulomb threshold, proportional to μ must be overcome—and therefore to a decrease of $\Delta_{max}(\Phi \rightarrow 2\pi)$ as μ increases, as observed in Fig. 5a.

In contrast, η appears constant over the wide range of μ, indicating robust performances in terms of dissipation. This is counter-intuitive because the dissipation of the stacked shells is expected to be mainly controlled by friction, without any major impact of snap-fit events. Note however that η purposefully quantifies the dissipation E_{diss} of the system normalised by the total injected energy $E_{in} \equiv F_{max}\Delta_{max}$. As such, the observed tiny dependence of η on μ could be interpreted as a cancellation between the effects of friction on the hysteresis E_{diss} and on Δ_{max}. Interestingly, we nonetheless observe that without friction (see the $\mu = 0$ data in Fig. 5), η significantly drops, indicating that the effect of friction on the hysteresis vanishes (Supplementary Fig. 3) while Δ_{max} saturates. Given that the value of η results from cooperative effects between the shells, additional theoretical efforts are necessary to predict η, which we leave as future work.

Based on the simulation, we can therefore conclude the following design principle for stacked shells: the combination of μ and Φ determines the maximum working distance, Δ_{max}, of the system. Given the value of Δ_{max}, we can require the set of μ and Φ, keeping the dissipation ratio η nearly constant.

Discussion

Our system exhibits a characteristic energy-absorbing behaviour, which could be exploited as a functional damper and energy absorber. The dissipation mechanism behind the stacked shells stems from the elasticity and geometry of shells, their contact mechanics, and their relative orientations. In this paper, we have studied the working distance and dissipation ratio (Δ_{max}, η) for the compression-decompression process. After the initial press, most of the possible shells have already snapped, leading the force-displacement curve to the limit cycle for $n \geq 2$. Even though shells do not snap so often at large n cycles, stacked shells are still flexible (through elastic bending). Given that conventional shock-absorbing materials exploit the collapse or fracture of their elements (voids, foams), the idea of stacking slender structures is useful in designing functional structures.

The mechanical metamaterials studied in the previous literature exhibit artificial mechanical performances upon compression, which primarily rely on programmed elementary structures. The defects and imperfections are, as such, critical in their mechanical performances[24]. The initial random orientations of the shells play, in our case, the role of such structural defects, and while the exact evolution of the system during compression depends on the initial conditions, the overall mechanical performances have been found to be quite robust. Hence, large deformation of slender structures can be utilised even when they are randomly stacked. Our study paves the way for new designing principles, where slender structures deform largely and relocate their positions from each other. We expect that a similar design idea will be applicable to engineering problems across different length scales from food packaging to the deformation of bowl-shaped molecules[25].

To directly compare our numerical and experimental results while reducing computational times, we have performed simulations for $N = 30$ shells. However, our simulation can still robustly simulate significantly larger systems, albeit at a high computational expense: systems composed of $N \sim 10^3$ shells for instance require, on a standard PC, about 9 days of computation per compression-decompression cycle, mainly owing to the very accurate resolution of frictional contact constraints required to prevent shell-shell penetrations and crossings. Obtaining reliable statistics for (Δ_{max}, η), therefore, requires much more computational power for large systems, and we leave the study of the thermodynamic limit ($N \gg 1$) as future work (c.f. section 'Statistics of Δ_{max} and η').

A fully analytical model would also provide a valuable and complementary approach towards the analysis of such large stochastic slender assemblies. Approaches based on statistical mechanics have proven successful in predicting random systems, such as molecular gases[26], granular particles[27] or active matter systems[28]. However, such kinetic approaches so far have been limited to rigid materials. Our experimental results will therefore be valuable to validate extended kinetic theories and models for largely deformable components.

To apply our idea on snap-fit between many shells in real engineering problems, the extension towards three-dimensional problems will be necessary. Once a 3D counterpart of stacked open shells is made, one can mimic the deformation of conventional cushioning materials such as stochastic foams[29]. Building such a complex model requires experimental and numerical modelling efforts, e.g., experimental contact visualisation or numerical contact modelling between shells, which we leave as a future study.

Methods

Fabrication of open cylindrical shells. Open cylindrical shells are casted in a thermoplastic way from naturally straight ribbons made of glycol-modified poly ethylene terephthalate. The straight ribbon is laser-cut into a length L and width $w = 10$ mm, from a flat sheet (Young's modulus, $E = 2.2$ GPa, thickness $h = 0.5$ mm, Shim Stock, Artus Corporation, USA). The total length of the ribbon, L, is varied in the range of $66.3 \leq L \leq 116.1$ mm, such that the shell angle $\Phi(=L/R)$ ranges $200° \leq \Phi \leq 350°$, meaning that $0.55 \leq \bar{\Phi} \leq 0.97$. The surface of the straight ribbon is roughened by sandpaper to reduce adhesive forces.

The mould for the open shells consists of two parts; outer and inner moulds. The acrylic outer mould has a circular hole, while the inner circular mould, which fits into the hole of the outer mould, is made of silicone elastomer (Smooth-on, USA). The straight ribbon is inserted between the outer and inner moulds such that the ribbon is bent into the uniform radius of curvature 19 mm. The set of a ribbon and mould is placed into the hot water of temperature 95 °C for more than 15 min. Subsequently, the ribbon and moulds are cooled in cold water (~20 °C) and then demoulded. The radius of curvature of the shell becomes $R = 19.2 \pm 0.2$ mm.

Experimental protocols for two-body problems. Two identical shells are compressed with each other quasi-statically at the speed of 0.17 mm s^{-1}. The middle of the shells is either fixed or connected to the force-testing machine (EZ-LX, Shimadzu, Japan). The former shell is fixed with the ground via an acrylic bar of 4 mm width. The latter shell is glued with an acrylic bar, which is clamped with the load cell.

Experimental protocols for randomly stacked shells. To prepare the initially stacked configuration, we randomly drop 30 shells one by one into the acrylic quasi-two-dimensional container ($200 \times 300 \times 11$ mm) by free-fall. The mechanical tests start at the initial height of the stacked shell under gravity, from which the zero of the displacement, $\Delta = 0$, is set. The shells are compressed and

decompressed by an acrylic plate of 8 mm width with a speed of 5 mm s^{-1}. The shells are compressed up to 5 N and then decompressed back to $\Delta = 0$. We iterate the compression/decompression cycles 10 times, against 5 different initial configurations. After completing each 10th cyclic test, we carefully examine the geometry of all the shells whether they are damaged or not. We regard the shells as damaged if the tips of the reference shell and those of the shells after the test differ by about 10h. If damaged shells are found, we apply the same protocol as section 'Fabrication of open cylindrical shells' prior to the next mechanical test.

Simulations

2D thin shells as 2D Kirchhoff rods. We represent our elastic shells in two dimensions using the two-dimensional Kirchhoff thin elastic rod model, which accounts for linear bending elasticity and exact geometrical non-linearities, at the origin of the large displacements of the rod[30]. To solve for the dynamics of this model, we develop a 2D, unclamped version of the high-order Super-Helix model, which has been originally popularised in Computer Graphics in the context of hair simulation[18], by taking the Poisson ratio into account in the re-scaling of the Young modulus. This model can be seen as a Galerkin (weak) discretisation of the Kirchhoff equations, composed of N helical elements with uniform material curvatures and twists. In 2D, the degrees of freedom of the rod boils down to N scalar curvatures, and each element takes the form of a circular arc. Compared to a nodal model, such a curvature-based model presents several advantages: the automatic capture of inextensibility, linear bending forces that can be integrated implicitly without additional cost, and a better speed of convergence with the number N of elements. In all the simulations performed in this paper, we took $N = 15$ elements for each rod, as we found this resolution sufficient for our accuracy needs.

Like the continuous 2D Kirchhoff rod model, the 2D Super-Helix model (namely the Super-Circle model) is parametrised by only four physical parameters: its length L, its natural curvature κ^0, its linear mass λ and its bending modulus B. When subject to gravity g, the model can be characterised by two dimensionless parameters: the gravitational bending parameter $\Gamma = \lambda g L^3 / B$ and the curliness $c = \kappa^0 L$. Note that in our experimental setting, the self-weight ~6×10^{-3} N is much smaller than the characteristic elastic bending forces $f_{Type I}$.

Dry frictional contact. To couple two elastic shells together, we model dry frictional contact through the Signorini–Coulomb law, which poses constraints on the admissible velocity and force at contact so that non-penetration and Coulomb friction conditions are satisfied. For the sake of simplicity, we only consider a single friction parameter μ, hence making no distinction between static and dynamic friction parameters. In our scenarios, we found that this single coefficient law was sufficient to yield very good agreements between experiments and simulations. We discretise the full, non-smooth dynamic problem of n contacting rods by using the Moreau time-stepping method[31], which resolves frictional contact constraints implicitly. In practice, we use the so-bogus library[32] which offers a free, robust, and efficient implementation of non-smooth frictional contact solvers based upon the hybrid algorithm first proposed by Daviet et al.[19]. We note that the coupling between the Super-Circle model and so-bogus has been carefully validated[20] on the stick-slip scenario of a straight indenting rod (pinning test), first introduced by Sano et al.[21]. We further improve the model by devising an arc-arc detection scheme, and validate our complete numerical model on a curved rod contacting a cylinder[12] (see Supplementary Note 1). For all our results, we used a time-step of 10^{-4} s, a solver tolerance of 10^{-16}(N s)^2 (square impulses) and a maximum number of iterations of 1000, allowing the solver to reach an accuracy of 10^{-9}(N s)^2 on average at each time-step.

The excellent agreements we obtain allow us, on the one hand, to calibrate precisely the frictional coefficient of our experimental shells by relying on simulation, using a shell-shell pinning experiment (see Fig. 2), and on the other hand, to compare successfully our 30-shell experiment to simulation results (see Figs. 3 and 4). Finally, our confidence in the numerical simulator allows us to conduct extensive parametric studies on the many-body scenario, in which we vary both the shell angle Φ and the friction coefficient μ, and use a set of 100 different initial conditions per simulation for robust statistical output data (see Fig. 5, next section and Supplementary Note 2). We conducted these simulations using the same protocol as the experimental one; in particular, we used the speed of 5 mm s^{-1} of the upper plate, which guarantees a quasi-static regime.

Statistics of Δ_{max} and η.
We observe experimentally and numerically that the Δ_{max} and η quantities measured on our 30-shell scenario are highly dependent on the initial configuration of the shell stack, which leads to some significant spreading in our results. A solution to reduce this spreading would be to scale up drastically the number of shells, both experimentally and numerically. Relying on a $\sqrt{N}$ law for the reduction of the distribution variance, we however anticipate that more than 10,000 shells would be necessary to yield less than 1% of spreading. Considering that our experimental shells are fabricated manually and that our simulation time raises from a few minutes for the first compression cycle of 30 shells to a few days for that of 1000 shells, this makes this approach currently intractable, both from an experimental and numerical point of view.

Instead, for the sake of efficiency, we stick to our small-scale 30-shell scenario and, for each pair (Φ, μ), we run in parallel 100 simulations featuring each a different random initial configuration. This allows us to build robust statistical data for Δ_{max}

and η across the variation of initial conditions. Our plots are summarised in Supplementary Fig. 2, for each (Φ, μ) pair considered. They all feature a Gaussian distribution, which confirms the ergodicity assumption of our system. Moreover, it is noteworthy that the variances are small, which allows us to report reasonably accurate averages for both quantities. For the experimental values ($\mu = 0.35$), it is noteworthy that our error bars are close to the experimental ones (see Fig. 5).

Data availability

Code availability

The codes for our numerical simulations are available upon request.

References

1. Gordon, J. E. *Structures: Or Why Things don't Fall Down* 2nd edn (Da Capo Press, Cambridge, 2003).
2. Lu, G. & Yu, T. *Energy Absorption of Structures and Materials* (Elsevier, New York, 2003).
3. Landau, L. D. & Lifshitz, E. M. *Theory of Elasticity* (Pergamon Press, 1980).
4. Bazant, Z. & Cendolin, L. *Stability of Structures: Elastic, Inelastic, Fracture and Damage Theories* (World Scientific, 1991).
5. Reis, P. M. A perspective on the revival of structural (in)stability with novel opportunities for function: from buckliphobia to buckliphilia. *J. Appl. Mech.* **82** https://doi.org/10.1115/1.4031456 (2015).
6. Holmes, D. P. Elasticity and stability of shape-shifting structures. *Curr. Opin. Colloid Interface Sci.* **40**, 118–137 https://doi.org/10.1016/j.cocis.2019.02.008 (2019).
7. Lakes, R. Foam structures with a negative poisson's ratio. *Science* **235**, 1038–1040 (1987).
8. Bertoldi, K., Reis, P. M., Willshaw, S. & Mullin, T. Negative poisson's ratio behavior induced by an elastic instability. *Adv. Mater.* **22**, 361–366 (2010).
9. Poincloux, S., Chen, T., Audoly, B. & Reis, P. M. Bending response of a book with internal friction. *Phys. Rev. Lett.* **126** https://doi.org/10.1103/PhysRevLett.126.218004 (2021).
10. Sano, T. G. & Wada, H. Snap-buckling in asymmetrically constrained elastic strips. *Phys. Rev. E* **97**, 013002 (2018).
11. Fu, K., Zhao, Z. & Jin, L. Programmable granular metamaterials for reusable energy absorption. *Adv. Funct. Mater.* **29** https://doi.org/10.1002/adfm.201901258 (2019).
12. Yoshida, K. & Wada, H. Mechanics of a snap fit. *Phys. Rev. Lett.* **125** https://doi.org/10.1103/PhysRevLett.125.194301 (2020).
13. Frenzel, T., Kadic, M. & Wegener, M. Three-dimensional mechanical metamaterials with a twist. *Science* **358**, 1072–1074 (2017).
14. Chen, T., Pauly, M. & Reis, P. M. A reprogrammable mechanical metamaterial with stable memory. *Nature* **589**, 386–390 (2021).
15. Silverberg, J. L. et al. Using origami design principles to fold reprogrammable mechanical metamaterials. *Science* **345**, 647–650 (2014).
16. Bertoldi, K., Vitelli, V., Christensen, J. & van Hecke, M. Flexible mechanical metamaterials. *Nat. Rev. Mater.* **2**, 17066 (2017).
17. Poirier, C., Ammi, M., Bideau, D. & Troadec, J.-P. Experimental study of the geometrical effects in the localization of deformation. *Phys. Rev. Lett.* **68**, 216–219 (1992).
18. Bertails, F. et al. Super-helices for predicting the dynamics of natural hair. *ACM Trans. Graph. (Proc. ACM SIGGRAPH'06)* **25**, 1180–1187 (2006).
19. Daviet, G., Bertails-Descoubes, F. & Boissieux, L. A hybrid iterative solver for robustly capturing Coulomb friction in hair dynamics. *ACM Trans. Graph. (Proc. ACM SIGGRAPH Asia'11)* **30**, 139:1–139:12 (2011).
20. Romero, V. et al. Physical validation of simulators in Computer Graphics: a new framework dedicated to slender elastic structures and frictional contact. *ACM Trans. Graph.* **40**, Article 66: 1–19 (2021).
21. Sano, T. G., Yamaguchi, T. & Wada, H. Slip morphology of elastic strips on frictional rigid substrates. *Phys. Rev. Lett.* **118**, 178001 (2017).
22. Andrade-Silva, I., Godefroy, T., Pouliquen, O. & Marthelot, J. Cohesion of bird nests. *EPJ Web Conf.* **249**, 06014 (2021).
23. Huber, P. J. *Robust Statistics* (Springer, 2011).
24. Evans, A. A., Silverberg, J. L. & Santangelo, C. D. Lattice mechanics of origami tessellations. *Phys. Rev. E* **92**, 013205 (2015).

25. Furukawa, S. et al. Ferroelectric columnar assemblies from the bowl-to-bowl inversion of aromatic cores. *Nat. Commun.* **12**, 768 (2021).
26. Lifshitz, E. M. & Pitaevskii, L. P. *Physical Kinetics* (Pergamon Press, 1981).
27. Brilliantov, N. V. & Pöschel, T. *Kinetic Theory of Granular Gases* (Oxford Univ Press, 2004).
28. Kanazawa, K., Sano, T. G., Cairoli, A. & Baule, A. Loopy lévy flights enhance tracer diffusion in active suspensions. *Nature* **579**, 364–367 (2020).
29. Evans, A., Hutchinson, J., Fleck, N., Ashby, M. & Wadley, H. The topological design of multifunctional cellular metals. *Prog. Mater. Sci.* **46**, 309–327 (2001).
30. Audoly, B. & Pomeau, Y. *Elasticity and Geometry: From Hair Curls to the Nonlinear Response of Shells* (Oxford University Press, 2010).
31. Moreau, J. Some numerical methods in multibody dynamics: application to granular materials. *Eur. J. Mech. – A/Solids* **13**, 93–114 (1994).
32. So-bogus library. https://gitlab.inria.fr/elan-public-code/so-bogus.

Author contributions
T.G.S., E.H., T.K., T.M., and F.B.-D. designed the research and interpreted the results. T.G.S. and T.K. performed experiments. F.B.-D. designed and implemented the unclamped super-helix model and E.H. and T.M. devised the circular arc detection algorithm. E.H. implemented the virtual 2D shell experiments and performed the numerical simulations, and T.M. and F.B.-D. supervised the numerical investigations. T.G.S. managed the project. T.G.S., T.M., and F.B.-D. wrote the paper.

Competing interests
The authors declare no competing interests.

Additional information
Supplementary information The online version contains supplementary material available at https://doi.org/10.1038/s43246-023-00383-2.

Correspondence and requests for materials should be addressed to Tomohiko G. Sano or Florence Bertails-Descoubes.

Peer review information *Communications Materials* thanks the anonymous reviewer(s) for their contribution to the peer review of this work. Primary Handling Editor: Aldo Isidori. A peer review file is available.

Reprints and permission information is available at http://www.nature.com/reprints

Publisher's note Springer Nature remains neutral with regard to jurisdictional claims in published maps and institutional affiliations.